Dislocation content of geometrically necessary boundaries aligned with slip planes in rolled aluminium

Hong, Chuanshi; Huang, Xiaoxu; Winther, Grethe

Published in:
Philosophical Magazine

Link to article, DOI:
10.1080/14786435.2013.805270

Publication date:
2013

Postprint
Philosophical Magazine, 2013 Vol. 93, No. 23, 3118–3141,
http://dx.doi.org/10.1080/14786435.2013.805270

Dislocation content of geometrically necessary boundaries aligned with slip planes in rolled aluminium

Chuanshi Hong[a]*, Xiaoxu Huang[a], Grethe Winther[b]

[a]*Danish-Chinese Center for Nanometals, Section for Materials Science and Advanced Characterization, Department of Wind Energy, Risø Campus, Technical University of Denmark, DK-4000, Roskilde, Denmark*

[b]*Department of Mechanical Engineering, Technical University of Denmark, DK-2800 Kgs. Lyngby, Denmark*

*Corresponding author. Tel: +45 46 77 58 76; FAX: +45 46 77 57 58; Email: chho@dtu.dk

Abstract

Previous studies have revealed that dislocation structures in metals with medium-to-high stacking fault energy depend on the grain orientation and therefore on the slip systems. In the present work, the dislocations in eight slip-plane-aligned geometrically necessary boundaries (GNBs) in three grains of near 45° ND rotated cube orientation in lightly rolled pure aluminium are characterized in great detail using transmission electron microscopy. Dislocations with all six Burgers vectors of the ½<110> type expected for fcc crystals were observed but dislocations from the four slip systems expected active dominate. The dislocations predicted inactive are primarily attributed to dislocation reactions in the boundary. Two main types of dislocation networks in the boundaries were identified: *i)* a hexagonal network of the three dislocations in the slip plane with which the boundary was aligned. Two of these come from the active slip systems, the third is attributed to dislocation reactions. *ii)* a network of three dislocations from both of the active slip planes. Two of these react to form Lomer locks. The results indicate a systematic boundary formation process for the GNBs. Redundant dislocations are not observed in significant densities.

Postprint
Philosophical Magazine, 2013 Vol. 93, No. 23, 3118–3141,
http://dx.doi.org/10.1080/14786435.2013.805270

Keywords

Dislocation boundaries; Dislocations; Slip systems; Transmission electron microscopy (TEM); Weak beam; Aluminium

1. Introduction

During plastic deformation of metals of medium to high stacking fault energy the gliding dislocations interact to give work-hardening and to form dislocation boundaries, which develop into a regular deformation microstructure within each grain. The microstructure evolves with strain and depends on temperature but a range of fcc [1–4] and bcc [5] metals exhibit microstructures with common characteristics. The dislocation boundaries in the microstructure may be parallel planar dislocation boundaries or cell boundaries [6]. The planar boundaries are believed to be geometrically necessary boundaries (GNBs). The cell boundaries are assumed to originate from statistically trapped dislocations and are also called incidental dislocation boundaries (IDBs).

The morphology of the dislocation boundary structure at low and intermediate strains ($0.05<\varepsilon<1$) has been classified into three main types [3]: Type 1 and Type 3 both have GNBs, in between which cells are found, together forming cell-blocks. Type 2 has no GNBs but only cell boundaries. The difference between Type 1 and Type 3 is the crystallographic alignment of the GNBs. In Type 1 structures the GNBs align with a slip plane and in Type 3 they align with other specific crystallographic planes [3,7].

The morphological type of the dislocation boundary structure depends strongly on the crystallographic orientation of the grain in which the structure evolves [3,8]. Recent research has furthermore shown that the type of dislocation boundaries formed can be predicted based on the slip systems expected to be active [9,10]. The strong relationship between the type of boundaries and the

Postprint
Philosophical Magazine, 2013 Vol. 93, No. 23, 3118–3141,
http://dx.doi.org/10.1080/14786435.2013.805270

active slip systems suggests that the dislocations in the boundaries are those coming from the active slip systems.

A recent study of the Type 2 structures in rolled Cube-oriented grains established that the dislocations in the eleven cell boundaries observed all had Burgers vectors corresponding to the two sets of codirectional slip systems active [11]. The aim of the present paper is to conduct an analogous experimental investigation of the slip-plane-aligned GNBs in Type 1 structures. Type 1 structures are typically found in tensile-deformed single-slip orientations and in rolled orientations with coplanar slip systems [3]. For example, the rolled Goss, Brass and 45° ND rotated cube orientations (ND refers to the normal direction of rolling) all have four active slip systems lying in two slip planes. The GNBs in these orientations align with the two active slip planes. The paper presents a detailed analysis of the dislocations in eight GNBs in three different grains of the 45° ND rotated cube orientation in 10% rolled pure aluminium.

2. Material and experimental methods

2.1 Material and deformation conditions

A high-purity Al (99.996%) sheet of 2 mm thickness was annealed at 300 °C for 2 h, resulting in an average grain size of 70 μm and a strong cube texture. Rectangular samples of dimensions 2×10×40 mm^3 were cut out to produce smaller sheets rotated 45° around the sheet normal. In these smaller sheets grains with orientations deviating less than 15° from the ideal 45° ND rotated cube orientation constitute more than 85% of the volume. These sheets were rolled to a thickness reduction of 10% in a single pass at room temperature, ensuring homogenous deformation [12]. In order to verify that well-defined GNBs have evolved, samples from the longitudinal section (containing the rolling and normal

directions) were characterized by electron channelling contrast (ECC) on a Supra 35 scanning electron microscope.

2.2 Sample sections and boundary planes

Detailed observations of the dislocation boundaries, including characterization of individual dislocations in the GNBs were carried out by transmission electron microscopy (TEM) on a JEOL 2000FX electron microscope, which was operated at a low voltage of 120 kV to minimize the damage induced by electron irradiation. Selection of the sample plane to observe is based on the following considerations: On one hand, an edge-on view, where the GNBs are perpendicular to the imaging plane, is required for the accurate determination of the GNB planes [13]. On the other hand, the dislocation content of a GNB can be determined only when the boundary dislocations are clearly revealed and well-separated, which requires the GNB to lie as parallel to the imaging plane as possible (here termed a flat-lying view). To obtain both viewing conditions the foil needs to be tilted by about 90°. Since the range of tilt is limited to ~±40° for our microscope (as well as for most conventional microscopes), an "intermediate" inclination at zero tilt seems the optimum so that both viewing positions can be obtained by tilting the foil within the available range. The two sets of GNBs in the 45° ND rotated cube orientation are inclined ±55° to the rolling plane and are parallel to the transverse direction of the rolling process (see Fig. 1). Both edge-on and nearly flat-lying viewing conditions of these GNBs can be obtained for foils taken from the rolling plane and mounted in the TEM with the transverse direction of rolling (TD) parallel to the tilt axis of the sample holder as illustrated in Fig. 2a. Consequently, the majority of the TEM foils are taken from the rolling plane. For comparison foils from the longitudinal plane were, however, also investigated.

Postprint
Philosophical Magazine, 2013 Vol. 93, No. 23, 3118–3141,
http://dx.doi.org/10.1080/14786435.2013.805270

2.3 Burgers vector determination

To examine the dislocation configurations and contributing Burgers vectors, **b**, in the GNBs, two-beam diffraction contrast experiments were carried out using different diffractions vectors, **g**. The weak-beam technique was employed using the (**g**/3**g**) diffraction condition to obtain sharp images. For each analyzed GNB, the dislocation configurations were represented by tracings of the corresponding two-beam diffraction contrast images. The colour scheme defined in Fig. 1b was used to designate the identity of the determined **b.** For convenience, hereafter the Burgers vectors $\pm\frac{1}{2}[10\bar{1}]$, $\pm\frac{1}{2}[01\bar{1}]$, $\pm\frac{1}{2}[1\bar{1}0]$, $\pm\frac{1}{2}[101]$, $\pm\frac{1}{2}[011]$ and $\pm\frac{1}{2}[110]$ are referred to as **b1**, **b2**… and **b6**, respectively. Note that slip on the four expected active slip systems involves glide of dislocations with **b1** and **b2** on (111) and **b4** and **b5** on $(11\bar{1})$.

The zone axes and diffraction vectors employed in the TEM were selected to provide the best flat-lying conditions for the GNB examined and also a range of diffraction vectors sufficient to identify the Burgers vectors using the $\mathbf{g}\cdot\mathbf{b}=0$ invisibility criterion [14] and assuming that only dislocations with Burgers vectors of the $\frac{1}{2}\langle 011\rangle$ type are present. The Kikuchi map in Fig. 2b illustrates the zone axes and diffraction vectors selected for the rolling-plane section. As indicated by the double-lined circles, the GNBs lying close to (111) were analyzed using mainly diffraction vectors from the $[\bar{1}\bar{1}2]$ zone axis, under which condition the foil was tilted by ~35° and the (111) plane lay nearly flat to the imaging plane. The thick-lined circles demonstrate that the GNBs near $(11\bar{1})$ were analyzed using mainly diffraction vectors from the $[11\bar{2}]$ zone axis, when the foil was tilted by ~-35° and the $(11\bar{1})$ lay nearly flat to the imaging plane. Besides, two diffraction vectors from the $[00\bar{1}]$ zone axis were used for both sets of GNBs, which corresponds to zero tilt of the foil and intermediate inclinations of the GNBs to the imaging plane.

Postprint
Philosophical Magazine, 2013 Vol. 93, No. 23, 3118–3141,
http://dx.doi.org/10.1080/14786435.2013.805270

A complete list of analysis conditions is found in Table 1, marking also the Burgers vectors that fulfil the $\mathbf{g}\cdot\mathbf{b}=0$ criterion and become invisible for each diffraction vector. Note that for many Burgers vectors shown in Table 1 the associated dislocations are expected to be out of contrast at two diffraction vectors. This is, for example, the case for three of the four Burgers vectors corresponding to the active slip systems when the boundaries are investigated in the rolling plane, both for the GNBs aligned with (111) and with $(11\bar{1})$. This means that the Burgers vector is unambiguously determined to be the one that is parallel to the cross product of the two diffraction vectors. Dislocations of the remaining Burgers vectors can also be uniquely identified from the combination of diffraction vectors, assuming that they are of the <011> type. It should be pointed out that no indications of dislocations of other types were found.

2.4 Dislocation line directions

The crystallographic directions of the dislocation lines were determined by employing the trace analysis technique [11,13]. The foil was viewed at different tilts in the microscope to find crystallographic planes that contain the dislocation line. In practice, an edge-on crystallographic plane whose trace coincides with the projected dislocation line on the image (trace direction) was found for each tilt. Once two such planes are found, the dislocation line direction is determined as the intersection line between the two planes.

3. Results

3.1 General microstructure

An example ECC micrograph of the deformed microstructures from the longitudinal section is shown

in Fig. 3a. Due to the sensitivity of ECC to grain orientation, the microstructure within some of the grains is not revealed. Nevertheless, pronounced GNBs are observed in the majority of the grains. In most cases two sets of intersecting GNBs are observed but some grains only have one pronounced set. For the grains with two sets of GNBs, in most cases one set is prominent and apparently more pronounced than the other; only in a few cases the two sets of GNBs appear equally developed.

In accordance with the ECC observations, TEM studies from both the rolling-plane and the longitudinal sections reveal GNBs. In the longitudinal section, the observed microstructures are analogous to those revealed by ECC, but with a better image resolution. Fig. 3b shows a microstructure within one grain, mainly consisting of two sets of well-defined straight GNBs, which intersect each other. In the rolling-plane section (Fig. 3c), fairly straight GNBs, which normally have a length of several to tens of micrometers, are found in all the grains observed. In general, these boundaries are aligned with TD. These observations are in good agreement with the expectation of two sets of GNBs with traces well separated by their opposite inclination to the rolling direction (RD) when observed in the longitudinal section, while the traces of both sets will be parallel to TD in the rolling plane.

3.2 GNBs selected for detailed characterisation

Based on the knowledge of the overall microstructure, a total of eight individual GNBs were selected for detailed TEM investigation. To illustrate the variations within one grain as well as variations between grains, six of the investigated GNBs are from the grain in the lower-right of Fig. 3c (referred to as Grain-1, with RD being [0.647 0.763 -0.003] and ND [-0.057 0.045 -0.997]), while the other two GNBs are from two other grains (Grain-2 with RD [0.795 0.606 -0.034] and ND [0.013 -0.073 -0.997], and Grain-3 with RD [0.735 0.678 -0.026] and ND [0.071 -0.114 -0.991]). To get the most complete picture observations were made in different sample sections, i.e. Grain-1 was observed in the rolling-

Postprint
Philosophical Magazine, 2013 Vol. 93, No. 23, 3118–3141,
http://dx.doi.org/10.1080/14786435.2013.805270

plane section and the other two in the longitudinal section.

The six GNBs investigated in Grain-1 are from two different parts of the grain and typical images are shown in Fig. 4a and 4b at tilts of ~35°, corresponding to the viewing condition illustrated in Fig. $2a_1$. Four GNBs (labelled GNB1-4) appear as rather wide bands, indicating that they are inclined to the imaging plane as would be the case for GNBs lying close to (111); while the other two GNBs (GNB5 and 6) lie near $(11\bar{1})$ and appear as sharp lines, as they are viewed nearly edge-on. Figure 4c is from Grain-2 in the longitudinal section and taken near zero tilt. The microstructure in Grain-2 mainly consists of a prominent set of GNBs that aligns with (111), and a secondary set that lies close to $(11\bar{1})$. The sharpness of the GNBs indicates that they are close to being edge-on. The segment of one of the GNBs enclosed in the white square and labelled GNB7 was investigated in detail. This GNB aligns with (111). The microstructure of Grain-3 (not shown here) is analogous to that of Grain-2, except that the microstructure of Grain-3 is dominated by GNBs that align with $(11\bar{1})$ instead of (111). A typical GNB (GNB8) aligning with $(11\bar{1})$ from Grain-3 was chosen for detailed observation.

The precise crystallographic planes of the eight selected GNBs were determined using the edge-on technique (for details of the technique, refer to [13]) and are listed in Table 2. To be brief, the alignment of a certain GNB is determined by tilting the TEM foil to a position where the GNB is exactly edge-on, i.e. the width of the boundary in the image is at a minimum, and comparing the GNB trace with the corresponding Kikuchi diffraction. To accurately determine the tilt position giving the minimum width a series of weak-beam images of each GNB was taken at different tilt angles (see supplementary Movies S1-3 for examples from GNB1-3). The misorientations across the GNBs are measured to be quite small, i.e. between 0.3° and 1.2°.

Postprint
Philosophical Magazine, 2013 Vol. 93, No. 23, 3118–3141,
http://dx.doi.org/10.1080/14786435.2013.805270

3.3 Dislocation networks and Burgers vectors

In the following the analysis of three of the selected GNBs aligned with (111) and one aligned with $(11\bar{1})$ will be presented in detail. The results for the remaining four GNBs are presented by comparison to the results from the first four.

As listed in Table 1 a total of six diffraction vectors were employed to characterize each GNB in the rolling plane and for the longitudinal plane four diffraction vectors were used. It is emphasized that the Burgers vectors of the boundary dislocations were deduced based on their visibility using the full range of diffraction conditions. For convenience, however, only images from a subset of the diffraction conditions are presented in the following, obviously those showing the greatest difference in terms of dislocation visibility.

3.3.1 GNB2 aligned with (111)

Figure 5 shows the dislocation content of GNB2 observed in the rolling plane. Figures $5a_1$-c_1 show typical weak-beam images using diffraction vectors of $[11\,\bar{1}\,]$, $[1\,\bar{3}\,1]$ and $[\,\bar{3}\,11]$, respectively. Figures $5a_2$-c_2 are tracings of the corresponding images where the Burgers vectors of the visible dislocations are illustrated using the colour code defined in Fig. 1. The dashed lines in the insets indicate the presence of dislocations invisible under the conditions used. Fig. 5d shows the entire dislocation network coloured according to the deduced Burgers vectors and Figs. 5e and 5f show typical dislocation configurations within the network.

Four prominent sets of dislocations with Burgers vectors **b1**, **b2**, **b3** and **b5** were identified: The dislocations with **b1** are visible in both Figs. $5a_1$ and $5c_1$, but invisible in Fig. $5b_1$; the **b2** dislocations are clearly revealed in Fig. $5a_1$ and $5b_1$, while they disappear in Fig. $5c_1$; and both the **b3** and **b5**

dislocations are out of contrast in Fig. $5a_1$ and in contrast in Figs. $5b_1$ and $5c_1$. The difference between **b3** and **b5** was established using **g**=[200], which is, however, not shown here. In addition, a few dislocations with **b6** are observed.

The **b1**, **b2** and **b3** dislocations in general form a hexagonal network, as evidenced by the differently oriented zigzag lines in Figs. $5a_1$-c_1, in which the three dislocation sets are made invisible one by one by the diffraction conditions. By contrast the **b5** dislocations form local rectangular grids with the **b1** dislocations, as most clearly seen in Fig. $5b_1$. Most of the dislocation line segments appear rather straight, and dislocations of the same Burgers vector are roughly parallel to each other.

3.3.2 GNB3 aligned with (111)

Figure 6 shows the dislocation content of GNB3 observed in the rolling plane, where Burgers vectors of **b1**, **b2**, **b5** and **b6** are present in significant densities. The dislocation network is dominated by a set of parallel dislocations with Burgers vector **b5**, as clearly seen from a comparison of Figs. $6a_1$ and b_1, in which **b5** dislocations are visible and invisible, respectively. As also revealed by Fig. $6b_1$ dislocations with **b6**, **b2** and **b1** are also present, forming zigzag lines.

The zigzag lines of **b1** and **b6** are part of a hexagonal network, with **b5** being the third dislocation in the hexagon. The **b5** dislocation segments in the hexagon are typically longer than the other two dislocation sets, making the hexagonal network elongated.

By contrast hexagonal networks involving **b2** dislocations are not regularly observed. Most of the **b2** dislocation segments intersect the **b5** dislocations, as seen in Figs. $6a_1$ and 6d. A few dislocations with **b4**, running parallel to the **b5** dislocations, are also observed. These **b4** dislocations often form nodes together with the **b2** and **b6** dislocations.

Postprint
Philosophical Magazine, 2013 Vol. 93, No. 23, 3118–3141,
http://dx.doi.org/10.1080/14786435.2013.805270

3.3.3 GNB7 aligned with (111)

Figure 7 shows the dislocation content of GNB7 observed in the longitudinal plane. Four dominant sets of dislocations, with Burgers vectors of **b1**, **b2**, **b4** and **b6** were identified (Figs. 7c and 7d). Two typical weak-beam images using diffraction vectors of [202] and $[11\bar{1}]$ are shown in Figs. 7a and 7b, respectively, where all the identified dislocations are visible in at least one of the images. The **b2**, **b4** and **b6** dislocations construct a hexagonal network, which is the dominant structure of the left-hand side of the images. On the right-hand side rectangular grids of **b1** dislocations and **b4** dislocations prevail. The two types of networks consititute two GNB segments which are inclined 13° to each other.

3.3.4 GNB8 near $(11\bar{1})$

The dislocation content of GNB8 as observed in the longitudinal section is shown in Fig. 8. Four prominent sets of dislocations, with Burgers vectors of **b2**, **b4**, **b5** and **b6**, respectively, were identified (Figs. 8d and 8e). A set of parallel **b2** dislocations dominates as clearly seen by comparison of Fig. $8a_1$ or $8b_1$ and $8c_1$, in which these dislocations are invisible and visible, respectively. By comparison of Fig. $8a_1$-c_1 it is seen that zigzag lines composed of **b4** and **b6** dislocations form an elongated hexagonal network with the **b2** dislocations, while less frequent segments of **b5** dislocations intersect the **b2** dislocations in a rectangular network. Some **b1** dislocations are also seen running parallel to the **b2** dislocations but they are very scarce.

3.4 Dislocation line directions and densities

The determination of dislocation line directions is illustrated for GNB1 in Fig. 9. For practical reasons, only the upper and lower parts of the GNB are analysed as these contain the most regular dislocation networks (see Fig. 9a). Given that all the boundary dislocations lie in the boundary plane of GNB1,

which has been determined to be (80 37 47) as listed in Table 2, determination of the line direction only requires identification of a second crystallographic plane that contains the dislocation line.

To facilitate the analysis, each dislocation line segment in Fig. 9a was approximated by a straight line and the trace direction of each such line was determined. The distribution of the trace directions for each set of dislocations is shown in Fig. 9c, where the direction is represented in terms of the angle ω between the horizontal direction and the trace in Fig. 9b. Clearly the distribution for each set of dislocations is narrow as quantified by the standard deviation, which is generally less than 10°. To simplify the procedure, the mean trace direction for each dislocation set is used to determine a second plane that "on average" contains the entire set of dislocations. By comparing the mean trace direction with the corresponding Kikuchi diffraction, the second planes that contain the **b1**, **b2**, **b3** and **b4** mean dislocation line traces were determined to be (-0.168 0.942 -0.290), (-0.933 0.257 0.253), (-0.653 -0.596 0.467) and (-0.741 -0.489 0.460), respectively. The intersection of these planes with the boundary plane of GNB1 was then determined as the mean line directions of the four sets of dislocations. The dislocation line directions were determined in the same manner for all the other GNBs investigated, and the results are listed in Table 3.

The measured line directions exhibit the characteristics of glide dislocations that remain on their slip plane. Dislocations gliding on the slip plane almost parallel to the GNB primarily have screw character (**b1** or **b2** in GNBs 1-4 and 7 aligned with (111); **b4** or **b5** in GNBs 5, 6 and 8 aligned with $(11\bar{1})$). By contrast, dislocations gliding on planes steeply inclined to the GNB have dislocation lines approximately coinciding with the intersection between the slip plane and the GNB. They are therefore roughly 60° dislocations (**b1** or **b2** in GNBs 5, 6 and 8 aligned with $(11\bar{1})$; **b4** or **b5** in GNBs 3, 4 and 7 aligned with (111)).

Postprint
Philosophical Magazine, 2013 Vol. 93, No. 23, 3118–3141,
http://dx.doi.org/10.1080/14786435.2013.805270

The planar density of each set of dislocations was also determined, which is defined as the sum of the true length of all dislocation segments of that set divided by the boundary area. The true length of a dislocation segment, l, is calculated according to $l=l'/\sin\alpha$, where l' is the projected length of the dislocation segment that is measured from the TEM image as illustrated in Fig. 9a, and α is the angle between the beam direction that is determined from Kikuchi diffraction and the true dislocation line direction as determined above. Similarly the boundary area is determined from the projected area that is measured from the TEM image and the angle between the beam direction and the normal to the boundary.

3.5 Summary of all GNBs

The dislocation content of the four GNBs presented in detail (GNB2, GNB3, GNB7 and GNB8) as well as the other four investigated GNBs (GNB1, GNB4, GNB5 and GNB6) is summarized in Fig. 10, in the form of tracings of the dislocation networks with the Burgers vector marked by colours according to the colour code in Fig. 1. The calculated dislocation densities for each boundary are shown Fig. 11.

As judged qualitatively from the TEM images and quantitatively demonstrated by the relatively small spread of the dislocation line directions in Fig. 9 the boundaries consist of well-defined dislocation networks where each set of dislocations are roughly parallel and fairly uniformly spaced. This suggests a systematic boundary formation process and enables further analysis of the boundary morphology, ending up with separation of the boundaries into two main categories.

The dominant configuration of GNB1 and GNB2 consists of a hexagonal grid of three sets of dislocations which is occasionally crossed by a fourth set. One should expect symmetrical equivalent boundaries aligned with $(11\bar{1})$ dominated by similar hexagonal grids of dislocations but these were not observed, probably due to the limited statistics.

The other main configuration is dominated by straight parallel dislocation lines of the same Burgers vector which are crossed by two other sets of dislocation lines of which one is straight and the other typically forms a zigzag line composed of two different Burgers vectors. This is the dominant network morphology of GNBs 3-8.

The combination of Burgers vectors in these networks is not unique, and all six Burgers vectors of the ½<110> type are observed. Note, however, that only GNB4 contains significant densities of dislocations with Burgers vectors from all of the expected active slip systems. The hexagonal networks only contain two of these, namely the dislocations from the slip plane with which the GNB aligns (plus an additional set from the same plane). The other main morphological configuration generally contains two sets of dislocations from the slip plane with which the GNB aligns and also dislocations from one of the slip systems on the other slip plane expected active.

4. Analysis and Discussion

4.1 Experimental conditions

In order to facilitate the analysis of dislocation content in the GNBs the experimental conditions must be chosen with care. A first criterion is to have GNBs that are well defined and consist of a regular network, in which individual dislocations are well separated. Previous studies using low-magnification TEM have revealed well-defined GNBs with traces extending over several micrometres after 5-10% deformation. Misorientation angles across slip-plane-aligned boundaries at a tensile strain of 10% have been reported to be about 0.8° [2], corresponding to an expected average spacing between the dislocations of about 30 nm, in good agreement with the present findings.

The purity of the material also plays a role. The GNBs in 99.5% pure aluminium (AA1050) have been demonstrated to have the same preferred crystallographic alignment as in purer material [3] but initial studies on AA1050 by the authors to reveal the individual dislocations showed that the dislocation network is much less defined. Previous studies of the dislocation content of deformation-induced boundaries have also been conducted on pure materials (see e.g. aluminium [11] and copper [15,16]).

Finally, the sample plane from which the TEM foil is taken must be considered. The rolling plane was selected for the majority of the present investigations as it is possible to view GNBs aligned with (111) as well as $(11\bar{1})$ with the GNBs being both edge-on and nearly flat-lying by tilting the foil ±35° around the transverse sample direction in the TEM. This gives the most precise determination of the crystallographic GNB plane and a projection with the best spatial separation of all dislocations with practically undistorted dislocation line directions.

It should be noted that the majority of studies of the general alignment of the GNBs are conducted in the longitudinal sample plane (e.g. [17–19]) as this is the plane in which the GNBs are viewed almost edge-on and the two sets of GNBs often present are well separated by having traces almost perpendicular to each other. Studies in other planes may be misinterpreted due to difficulties in resolving the two different traces if not conducted at sufficient resolution [20].

For comparison with the rolling-plane observations two of the GNBs in the present study were characterized in the longitudinal plane, by tilting the foil about 30° along a Kikuchi band that steeply inclines to the boundary trace on the TEM to a give a projection of the GNB plane which is roughly 60° inclined to the viewing plane. In practice this turned out to work well due to the fairly large separation of the dislocations in the boundary, but when analysing these images one must correct for the

distortions caused by the projection. More specifically the dislocation line length and spacing in the normal direction of the foil (i.e. the short dimension of the boundary networks in GNBs 7 and 8) is reduced by a factor of two in this projection.

In the present work, studies in a sample plane almost parallel to one of the GNB planes were also attempted, following a suggestion made in [21], but in reality it turned out to be virtually impossible to find a GNB due to the fact that the distance between the GNBs is of the order of micrometres which is many times the thickness of the TEM foil.

In summary, pure metals deformed to strains of about 0.1 and viewed in a sample section which can produce both edge-on and flat-lying projections by tilting around a well-selected axis on the TEM provide the optimum conditions for this type of study. For most orientations the rolling-plane section and tilting around TD will be the best due to the general macroscopic alignment of the boundaries (e.g. [6,20,22–24]). It is a further requirement that a sufficient combination of diffraction vectors is available in order to deduce the Burgers vectors. Ideally, invisibility at two different diffraction vectors is needed to make an unambiguous determination but with the assumption of dislocations being of the ±1/2<110> type only, fewer diffraction vectors may be employed. Suitable combinations of zone axes and diffraction vectors depend on the actual grain orientation studied.

4.2 GNB planes

Although the low-magnification TEM images in Figs. 3c and 4c show a fairly close GNB alignment with the traces of the (111) and $(11\bar{1})$ planes, and the sharpness of the boundaries in especially Fig. 4 indicates that the boundaries are close to edge-on conditions in agreement with rough alignment with the slip planes, this alignment is not perfect. It is well-established that the GNBs always deviate a little from the exact slip planes even in tensile-deformed single crystals oriented for single slip [25]. The

rotation of GNBs away from the slip plane has further been found to vary systematically with the crystal/grain orientation [7,25]. The strain level [20] and solute/impurity content [3,20] have also been reported to have some influence. In particular the GNBs in a channel-die compressed single crystal of pure aluminium (99.99%) of brass orientation were found to deviate more from the slip plane at a strain of 0.15 than at 0.5 [20], and the GNBs in nine grains of near-brass orientation in a rolled 99.5 % pure aluminium at a strain of 0.33 were found to deviate less than 7° from the slip plane [3]. Understanding the deviations are of importance for theories of boundary formation mechanisms [25,26] as well as for the mechanical contribution from slip-plane-aligned GNBs [27].

Previous studies of slip-plane-aligned GNBs have also shown that a GNB often consists of smaller parallel segments that are on the {111} slip plane, which are connected by even smaller segments obviously not on the {111} plane [3]. A recent study of dislocation boundaries in a Goss-oriented grain in rolled nickel by 3D-EBSD has found that the GNBs were quite wavy, especially along TD [28,29]. This has also been observed when comparing observations in the rolling-plane and longitudinal sections (see also Figs. 3 and 4), but has often been attributed to viewing conditions being far from edge-on condition in the rolling-plane section and interference patterns caused by the presence of two GNBs with almost the same trace in this section [21].

The high magnification required to resolve individual dislocations means that only small segments of a GNB can be characterized at a time and in fact all the presently analysed segments are from different boundaries. As listed in Table 2 GNB1 and GNB2 deviate the most (up to 28°) from the exact {111} plane while the deviations for the remaining GNBs are smaller than 11°. Due to the limited statistics it was not possible to draw any conclusions on the differences between the observations in the rolling-plane and longitudinal sections. It is, however, clear that the GNBs consist of slightly

misoriented segments when viewed over distances longer than those investigated here. In fact the investigated GNB2 and GNB7 both encompass of two smaller planar segments as illustrated in Fig. 12 for GNB2 and also indicated in Table 2. As seen from the tracings of the dislocation networks in these GNBs in Figs. 5 and Fig.7 there is some variation for these two GNBs along the characterised boundary. The middle part of GNB2, which is the interconnecting region in Fig. 12, has a much more irregular dislocation network than the upper and lower parts corresponding to the two smaller planar segments in Fig. 12. The left and right parts of GNB7, which have different morphologies of the dislocation network, are also two different smaller segments, as indicated in Fig. 7c. These findings suggest that the segments at least in part arise because of local fluctuations in the dislocation content and therefore probably local fluctuations of the slip activities.

4.3 Slip systems, Burgers vectors and dislocation reactions

As shown in Figs. 10 and 11, most of the observed dislocations in the boundaries have Burgers vectors corresponding to the expected active slip directions, i.e. **b1**, **b2**, **b4** and **b5**. This is in good agreement with the fact that the type of dislocation boundaries, in particular their crystallographic alignment, depends on the grain orientation and further correlates with the expected slip.

Nevertheless, it is also clear that dislocations with the two other Burgers vectors relevant for fcc metals are well-represented, namely **b3** and **b6**, as shown in Fig. 11 in terms of the dislocation density. Their occurrence may either be attributed to activation of more than the initially expected four slip systems or to reactions between the dislocations gliding on these four slip systems.

The four slip systems expected active on the two slip planes indicated in Fig. 1 have identical Schmid factors with the high value of 0.41. Four other slip systems have Schmid factors of 0.20 but these are the cross slip systems of those with the highest Schmid factors and therefore do not contribute

dislocations with new Burgers vectors. The slip systems on which dislocations with **b3** and **b6** would glide have Schmid factors of 0. It is further noted that the Taylor model predicts the four systems with the highest Schmid factors to be equally active with no additional active systems. Activation of systems giving rise to dislocations with **b3** and **b6** would lead to neither compression nor elongation along any of the main deformation axes, ND or RD, but only to shear strain components.

To investigate this further the Burgers vectors of several dislocations observed outside the GNBs were determined. These were all found to belong to one of the four systems expected active. It should, however, be noted that the presence of long dislocations lines with Burgers vector **b6**, which apparently extends outside the boundary network of GNB3 may indicate slip on other systems. Unfortunately, the tilting sequence conducted to determine the boundary plane was performed with diffraction conditions making these dislocations invisible, meaning that three-dimensional information about this part of the dislocations (incl. glide plane analysis) is not available. In general, activation of other systems than the two sets of coplanar ones is, however, probably not the reason for the observation of dislocations with **b3** and **b6**.

For two crossing dislocations with Burgers vectors $\mathbf{b_a}$ and $\mathbf{b_b}$ reaction will occur if it leads to a reduction in energy of the entire configuration [30]. For fcc crystals this is fulfilled for two dislocations gliding on the same slip plane, i.e. reaction between **b1** and **b2** is favoured and results in **b3** dislocations. By analogy reactions between **b4** and **b5** giving **b3** are expected. A dislocation node joining three screw dislocations with 120° between the dislocation lines is at equilibrium [30]. Formation of the observed regular hexagonal grid is therefore energetically favourable. The facts that the numbers of **b1**, **b2** and **b3** dislocation segments are similar to each other (~1/3 of the total number

of dislocation segments) in both GNB1 and GNB2, and that **b3** dislocations are only present in significant numbers in these two boundaries, suggest the occurrence of such dislocation reactions.

Energetically favourable dislocation reactions may also occur between dislocations gliding on two different slip planes. Reactions between **b2** and **b4** (or **b1** and **b5**) may give dislocations of **b6**. If the reacting dislocations move by glide only they will meet at the intersection line between the two slip planes, which will also be the dislocation line of the reaction product **b6**. This line is perpendicular to **b6** and as the Burgers vector and the dislocation line do not lie in the same {111} plane the reaction product is a sessile Lomer lock [30]. Note that **b6** dislocations are observed in GNBs 3-8 but are scarcely found in GNB1 and GNB2, which is in accordance with the possible dislocation reactions in the boundaries.

McCabe et al. [16] characterized the dislocations in a single slip-plane-aligned GNB in a rolled near-Brass-oriented grain in rolled copper. This orientation is also expected to slip on two sets of coplanar systems but not as symmetrically as in the presently investigated 45° ND rotated cube orientations. In the study by McCabe et al. the boundary dislocations were also found to come from the active systems and Lomer locks were observed. The spatial arrangement, however, was a rectangular grid with dislocation lines differing from those found in the present study. The rectangular dislocation grid was found to fulfil the Frank equation [31,32] for boundaries free of long-range stresses. Wei et al. [11] found that the dislocation configurations in eleven similarly oriented cell boundaries investigated in rolled aluminium grains of near cube orientation were all identical square grids, for which the Frank equation was also fulfilled. A more comprehensive study of the presently determined dislocation content in relation to the Frank equation is outside the scope of the present paper and will be presented in a subsequent publication.

Postprint
Philosophical Magazine, 2013 Vol. 93, No. 23, 3118–3141,
http://dx.doi.org/10.1080/14786435.2013.805270

4.4 Dislocation densities

The misorientation angle across a GNB is related to the dislocation density in the GNB [30]. The total planar density of dislocations in GNB8 was measured to be 4.5×10^{7} m^{-1} from the diffraction contrast images. This dislocation density corresponds to a misorientation of 0.74° for a tilt boundary with one set of edge dislocations and 0.37° for a twist boundary with two crossed dislocations or a hexagonal network of three dislocations. With an accuracy of ~0.1° the misorientation across GNB8 was measured to be 0.55-0.62° using recorded Kikuchi patterns, which falls in between the value for a tilt boundary and that of a twist boundary. The misorientation axis across GNB8 is [-0.84, 0.47, 0.28] or [-0.86, 0.32, 0.39] as obtained by two repeated measurements, corresponding to a mixed tilt-twist character of the boundary. An analogous analysis was conducted for GNB7 with the same conclusion. It is therefore concluded that virtually all dislocations in the GNB are necessary in the sense that they contribute to the crystallographic misorientation.

It is commonly found that stored energies calculated from TEM characterisation of the spacing between dislocation boundaries and their misorientation angles are a factor of about two lower than the stored energies measured by calorimetry [33]. This has been attributed to the presence of significant densities of redundant dislocations not contributing to the misorientation. This interpretation is not supported by the present findings for rolled aluminium.

5. Conclusions

Detailed TEM investigations of eight planar geometrically necessary boundaries in three grains of the 45° ND rotated cube orientation in 10% rolled 99.996% pure Al were carried out. Four slip systems on two slip planes are expected active and the two sets of GNBs observed align with these, although not perfectly. The activation of two sets of coplanar slip systems and the slip-plane-aligned boundaries are

typical for the α-fibre of the stable fcc rolling texture, although the orientation itself is not stable. Five of the boundaries were aligned with the (111) slip plane and the other three aligned with $(11\bar{1})$.

- Dislocations with all six Burgers vectors of the ½<110> type expected for fcc crystals were observed but dislocations from the four active slip systems dominated. The dislocations with Burgers vectors not corresponding to one of the expected active slip systems are primarily believed to be the result of dislocation reactions in the boundary.
- The dislocation content of the eight GNBs was not the same, and only one contained Burgers vectors from all of the four slip systems expected active. However, two main types of dislocation networks in the boundaries were identified:
    - 3 sets of dislocations in a hexagonal network all having Burgers vectors in the slip plane with which the boundary aligned. Two of these come from the active slip systems, the third is attributed to dislocation reactions.
    - 3 sets of dislocations from the active slip systems, of which two react to form Lomer locks. Two of the slip systems lie in the plane with which the GNB aligns, the third system comes from the other active slip plane.
- The dislocation density in the GNBs is in good agreement with the density calculated based on the misorientation angle across the boundaries, i.e. redundant dislocations are not present in significant quantities. Further analysis of the dislocation content in relation to the Frank equation for boundaries free of long-range stresses is in progress.

Supplementary movies are available online alongside with this article.

Acknowledgements

The authors gratefully acknowledge support from the Danish National Research Foundation and the National Natural Science Foundation of China (Grant No. 51261130091) for the Danish-Chinese Center for Nanometals, within which this work was performed. The authors thank N. Hansen and A. Godfrey for valuable comments on the manuscript, and E. Johnson, A. Ramar and T. Yu for helpful discussions on the TEM experiments.

References

[1] N. Hansen and D. Jensen, Philos. Trans. R. Soc. Lond. Ser. A - Math. Phys. Eng. Sci. 357 (1999) p.1447.

[2] N. Hansen, X. Huang, W. Pantleon and G. Winther, Phil. Mag. 86 (2006) p.3981.

[3] X. Huang and G. Winther, Phil. Mag. 87 (2007) p.5189.

[4] P. Landau, G. Makov, R.Z. Shneck and A. Venkert, Acta Mater. 59 (2011) p.5342.

[5] A. Haldar, X. Huang, T. Leffers, N. Hansen and R. Ray, Acta Mater. 52 (2004) p.5405.

[6] B. Bay, N. Hansen, D.A. Hughes and D. Kuhlmann-Wilsdorf, Acta Metall. Mater. 40 (1992) p.205.

[7] G. Winther, X. Huang and N. Hansen, Acta Mater. 48 (2000) p.2187.

[8] F.X. Lin, A. Godfrey and G. Winther, Scr. Mater. 61 (2009) p.237.

[9] G. Winther and X. Huang, Phil. Mag. 87 (2007) p.5215.

[10] G. Winther, Acta Mater. 56 (2008) p.1919.

[11] Y.L. Wei, A. Godfrey, W. Liu, Q. Liu, X. Huang, N. Hansen et al., Scr. Mater. 65 (2011) p.355.

[12] O. Mishin, B. Bay, G. Winther and D. Jensen, Acta Mater. 52 (2004) p.5761.

[13] X. Huang and Q. Liu, Ultramicroscopy 74 (1998) p.123.

[14] D.B. Williams and C.B. Carter, *Transmission Electron Microscopy,* Plenum Press, New York, 1996.

[15] D. Hughes, S. Khan, A. Godfrey and H. Zbib, Mater. Sci. Eng. A - Struct. 309 (2001) p.220.

[16] R. McCabe, A. Misra and T. Mitchell, Acta Mater. 52 (2004) p.705.

[17] P. Cizek, F. Bai, E. Palmiere and W. Rainforth, J. Microsc.-Oxford 217 (2005) p.138.

[18] A. Borbely, C. Maurice, D. Piot and J.H. Driver, Acta Mater. 55 (2007) p.487.

[19] A.S. Taylor, P. Cizek and P.D. Hodgson, Acta Mater. 60 (2012) p.1548.

[20] A. Albou, J.H. Driver and C. Maurice, Acta Mater. 58 (2010) p.3022.

[21] G. Winther, X. Huang, A. Godfrey and N. Hansen, Acta Mater. 52 (2004) p.4437.

[22] H. Christoffersen and T. Leffers, Acta Mater. 46 (1998) p.4093.

[23] P.J. Hurley, P.S. Bate and F.J. Humphreys, Acta Mater. 51 (2003) p.4737.

[24] G. Winther, Acta Mater. 51 (2003) p.417.

[25] Y. Kawasaki, in *Strength of Materials. Fundamental Physical Aspects of the Strength of Crystalline Materials. ICSMA 10,* H. Oikawa, K. Maruyama, S. Takeuchi and M. Yamaguchi, eds., Japan Institute of Metals, Sendai, 1994, p.231.

[26] P.J. Jackson, Prog. Mater. Sci. 29 (1985) p.139.

[27] G. Winther, Scr. Mater. 52 (2005) p.995.

[28] N. Afrin, M.Z. Quadir, L. Bassman, J.H. Driver, A. Albou and M. Ferry, Scr. Mater. 64 (2011) p.221.

[29] N. Afrin, M.Z. Quadir, W. Xu and M. Ferry, Acta Mater. 60 (2012) p.6288.

[30] J.P. Hirth and J. Lothe, *Theory of dislocations,* McGraw-Hill, New York, 1968.

[31] F.C. Frank, in *Symposium on Plastic Deformation of Crystalline Solids,* Mellon Institute of Industrial Research, Pittsburgh, 1950, p.150.

[32] F.C. Frank, Phil. Mag. 42 (1951) p.809.

[33] T. Knudsen, W.Q. Cao, A. Godfrey, Q. Liu and N. Hansen, Metall. Mater. Trans. A - Phys. Metall. Mater. Sci. 39A (2008) p.430.

Postprint
Philosophical Magazine, 2013 Vol. 93, No. 23, 3118–3141,
http://dx.doi.org/10.1080/14786435.2013.805270

Table 1 Selection of zone axes and diffraction vectors for Burgers vector analysis of GNB dislocations, considering the GNB alignment and sample sectioning direction.

GNBs aligned with (111)									GNBs aligned with $(11\bar{1})$								
Zone axis	**g**	**g·b** for different **b**s							Zone axis	**g**	**g·b** for different **b**s						
		b1 $10\bar{1}$	**b2** $01\bar{1}$	**b3** $1\bar{1}0$	**b4** 101	**b5** 011	**b6** 110	/2			**b1** $10\bar{1}$	**b2** $01\bar{1}$	**b3** $1\bar{1}0$	**b4** 101	**b5** 011	**b6** 110	/2
Rolling-plane section: GNB1-GNB4									*Rolling-plane section: GNB5-GNB6*								
$\bar{1}\bar{1}\bar{2}$	$2\bar{2}0$	1	-1	2	1	-1	0		$11\bar{2}$	$2\bar{2}0$	1	-1	2	1	-1	0	
	$11\bar{1}$	1	1	0	0	0	1			111	0	0	0	1	1	1	
	$1\bar{3}1$	0	-2	2	1	-1	-1			$3\bar{1}1$	1	-1	2	2	0	1	
	$\bar{3}11$	-2	0	-2	-1	1	-1			$1\bar{3}\bar{1}$	1	-1	2	0	-2	-1	
$00\bar{1}$	200	1	0	1	1	0	1		$00\bar{1}$	200	1	0	1	1	0	1	
	020	0	1	-1	0	1	1			020	0	1	-1	0	1	1	
Longitudinal section: GNB7									*Longitudinal section: GNB8*								
$1\bar{2}\bar{1}$	202	0	-1	1	2	1	1		$0\bar{3}1$	113	-1	-1	0	2	2	1	
	$11\bar{1}$	1	1	0	0	0	1		$1\bar{2}1$	111	0	0	0	1	1	1	
$0\bar{1}0$	200	1	0	1	1	0	1		$0\bar{1}0$	200	1	0	1	1	0	1	
	002	-1	-1	0	1	1	0			002	-1	-1	0	1	1	0	

Postprint
Philosophical Magazine, 2013 Vol. 93, No. 23, 3118–3141,
http://dx.doi.org/10.1080/14786435.2013.805270

Table 2 Determined boundary planes of the GNBs.

		GNB plane determined experimentally	Nearest {111}	GNB plane deviation from {111}
Rolling-plane section	GNB1	(80 37 47)	(111)	18°
	GNB2 Seg1*	(76 54 37)	(111)	16°
	Seg2	(88 42 24)	(111)	28°
	GNB3	(63 60 50)	(111)	6°
	GNB4	(49 61 62)	(111)	6°
	GNB5	(46 63 -62)	$(11\bar{1})$	8°
	GNB6	(47 69 -55)	$(11\bar{1})$	9°
Longitudinal section	GNB7 Seg1*	(55 44 71)	(111)	11°
	Seg2	(69 48 54)	(111)	9°
	GNB8	(55 54 -64)	$(11\bar{1})$	4°

*For GNB2 and GNB7, the characterized GNB consists of smaller planar segments, and accordingly the boundary plane is determined for each smaller segment.

Postprint
Philosophical Magazine, 2013 Vol. 93, No. 23, 3118–3141,
http://dx.doi.org/10.1080/14786435.2013.805270

Table 3 Summary of dislocation line directions in the GNBs.

		b1, $[10\bar{1}]/2$		**b2**, $[01\bar{1}]/2$		**b3**, $[1\bar{1}0]/2$		**b4**, $[101]/2$		**b5**, $[011]/2$		**b6**, $[110]/2$	
		$\bar{\xi}$ *	$\angle \mathbf{b}\bar{\xi}$ ** (°)	$\bar{\xi}$	$\angle \mathbf{b}\bar{\xi}$ (°)	$\bar{\xi}$	$\angle \mathbf{b}\bar{\xi}$ (°)	$\bar{\xi}$	$\angle \mathbf{b}\bar{\xi}$ (°)	$\bar{\xi}$	$\angle \mathbf{b}\bar{\xi}$ (°)	$\bar{\xi}$	$\angle \mathbf{b}\bar{\xi}$ (°)
GNBs aligned with (111)	GNB1	[56 -15 -82]	14	[3 76 -65]	5	[53 -80 -28]	20	[48 -86 -14]	76				
	GNB2 Seg1	[46 -5 -88]	17	[-15 69 -71]	9	[64 -73 -25]	15						
	Seg2	[26 1 -96]	30	[-16 73 -66]	10	[48 -76 -43]	28			[-48 71 52]	30		
	GNB3	[39 31 -87]	27	[2 63 -78]	6			[75 -65 -16]	65	[-75 65 16]	55	[61 -78 17]	83
	GNB4	[75 7 -66]	5	[6 69 -72]	4			[77 -64 3]	56	[-77 64 -3]	64	[87 -40 -29]	71
	GNB7 Seg1	[67 29 -69]	17	[-22 90 -39]	25			[67 -74 -6]	64			[84 -28 -47]	67
	Seg2	[69 -23 -68]	13	[-12 81 -57]	12			[57 -82 -1]	67			[70 -61 -36]	86
GNBs aligned with $(11\bar{1})$	GNB5	[81 -58 1]	56	[83 -56 4]	65			[64 25 73]	15	[3 69 73]	2	[55 -75 -36]	82
	GNB6			[-83 56 0]	67					[-18 68 71]	10	[73 -65 -21]	87
	GNB8	[69 -73 -3]	60	[-72 69 -4]	59			[61 26 75]	16	[6 74 67]	4	[42 -84 -34]	73

* $\bar{\xi}$: average dislocation line direction;

** $\angle \mathbf{b}\bar{\xi}$: angle between **b** and $\bar{\xi}$.

Postprint
Philosophical Magazine, 2013 Vol. 93, No. 23, 3118–3141,
http://dx.doi.org/10.1080/14786435.2013.805270

Figures

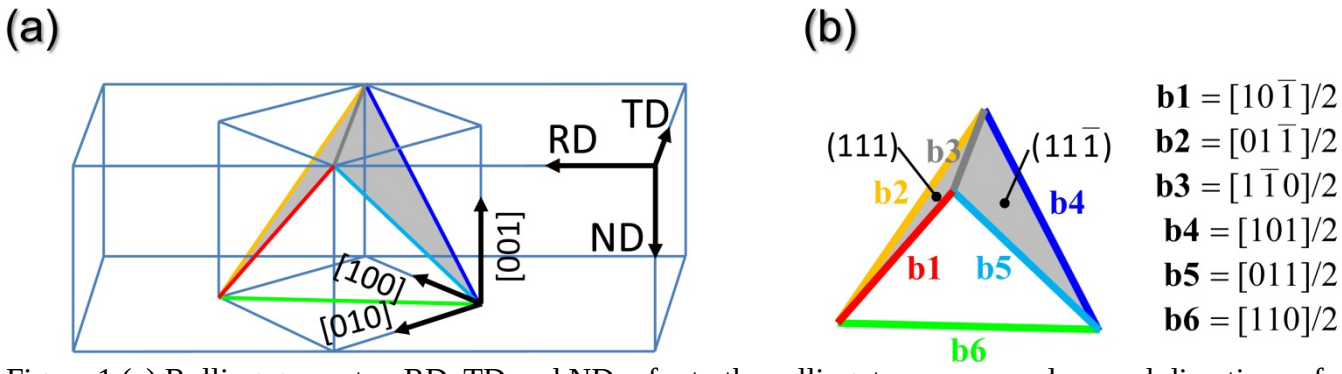

Figure 1 (a) Rolling geometry. RD, TD and ND refer to the rolling, transverse and normal directions of rolling geometry, respectively. Slip planes of the coplanar slip systems predicted active are colored gray. (b) Color code for schematic illustration of dislocations based on their Burgers vectors.

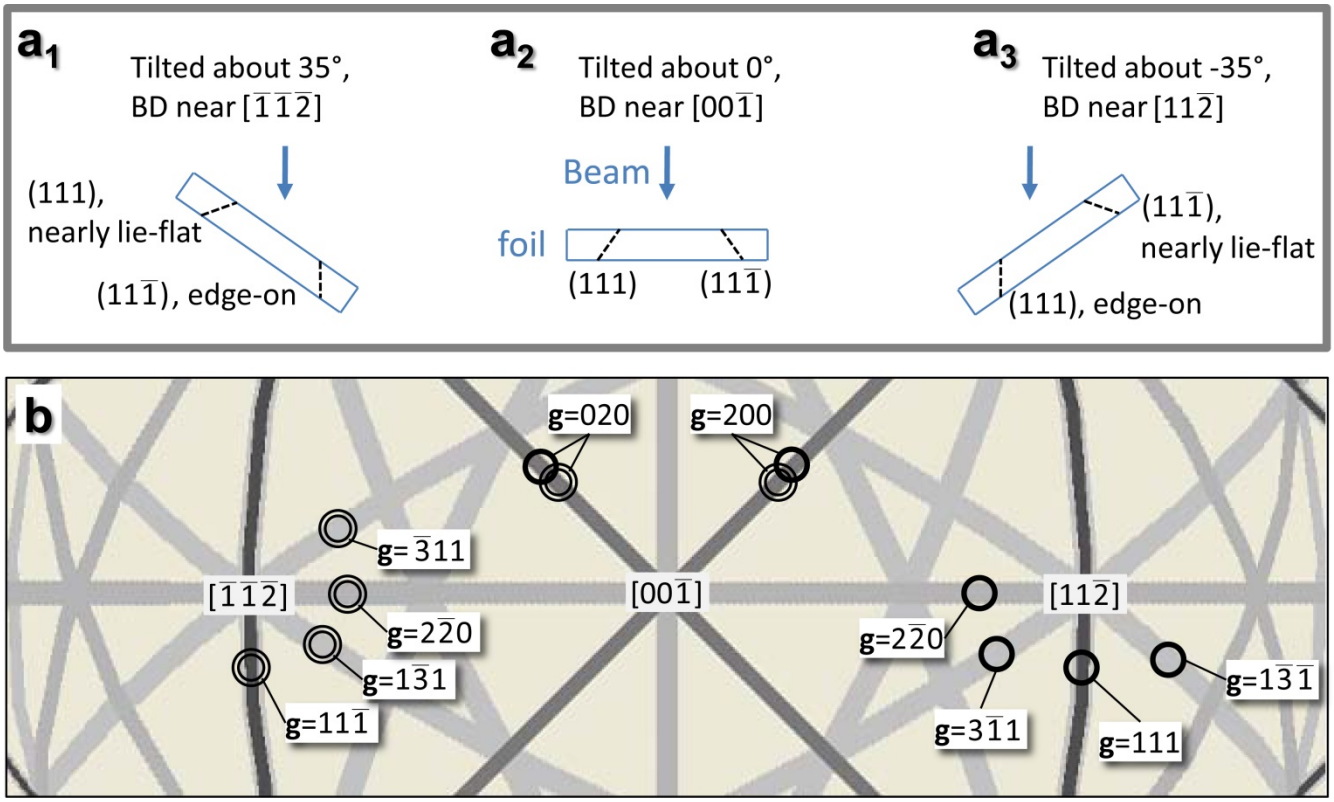

Figure 2 (a_1-a_3) Inclination of predicted GNBs relative to beam direction (or imaging plane) in TEM at different tilt positions, for foils prepared from the rolling-plane section. The rectangular frames

Postprint
Philosophical Magazine, 2013 Vol. 93, No. 23, 3118–3141,
http://dx.doi.org/10.1080/14786435.2013.805270

represent the foil whereas the dashed lines represent the GNBs. (b) Selection of diffraction vectors for Burgers vector analysis, considering the GNB inclinations in the foil. The thick-lined circles and double-lined circles indicate diffraction vectors used for GNBs aligned with $(11\bar{1})$ and those aligned with (111), respectively.

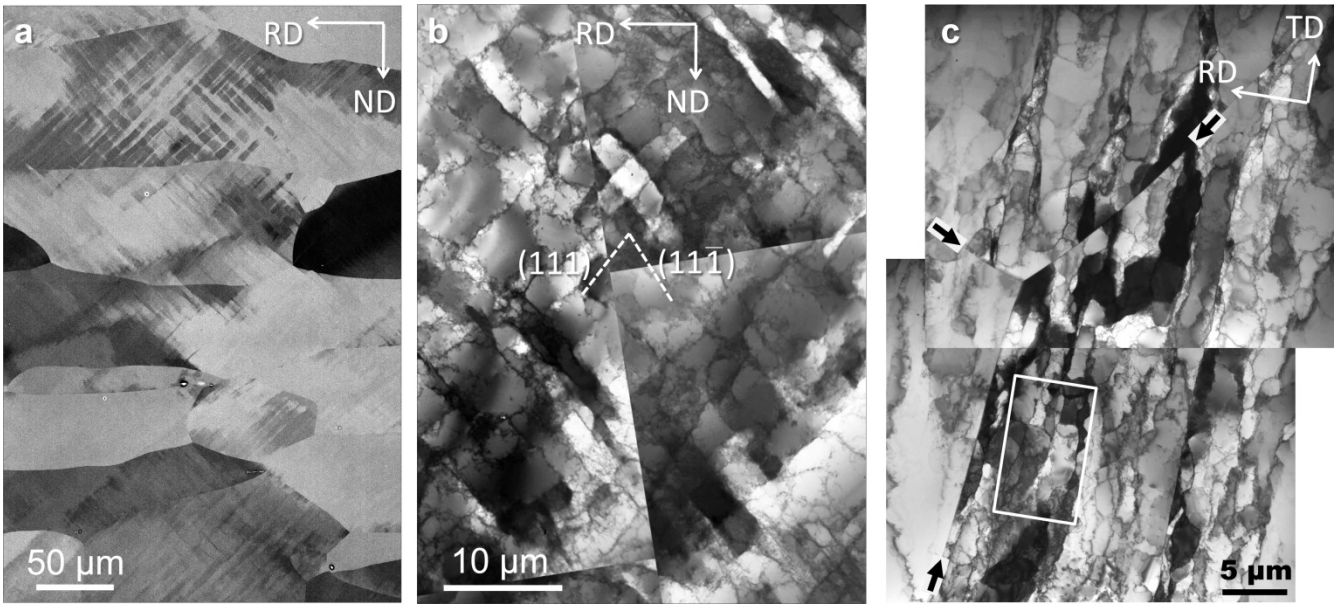

Figure 3 (a) ECC observation of the deformed microstructure from the longitudinal section. (b,c) TEM observations of the deformed microstructure from the longitudinal section (b) and the rolling-plane section (c). The dashed lines in (b) indicate the traces of (111) and $(11\bar{1})$ slip planes. The black arrows in (c) indicate the coarse-grain boundaries and the white rectangle outlines a region observed closer in Fig. 4a.

Postprint
Philosophical Magazine, 2013 Vol. 93, No. 23, 3118–3141,
http://dx.doi.org/10.1080/14786435.2013.805270

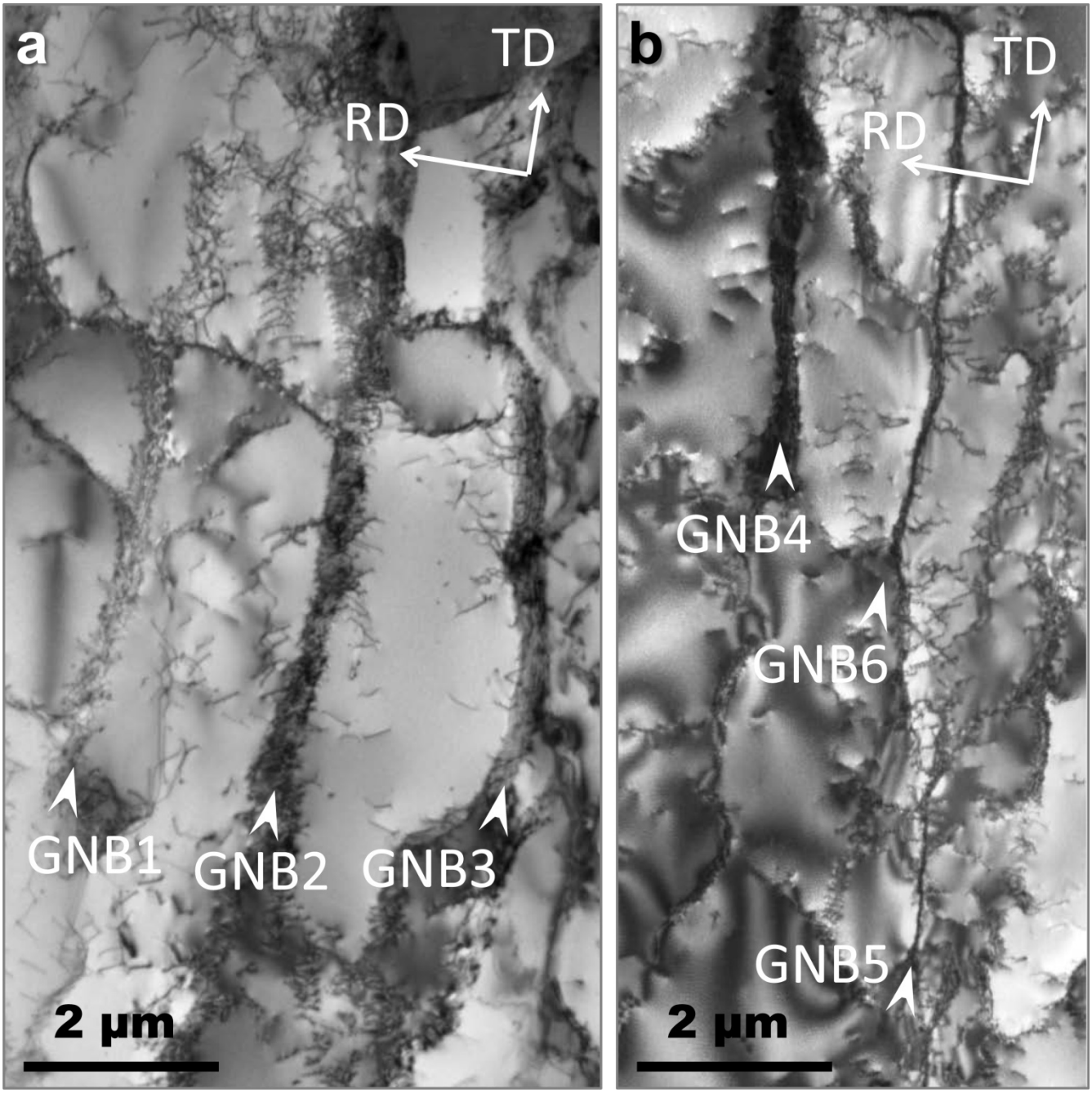

Postprint
Philosophical Magazine, 2013 Vol. 93, No. 23, 3118–3141,
http://dx.doi.org/10.1080/14786435.2013.805270

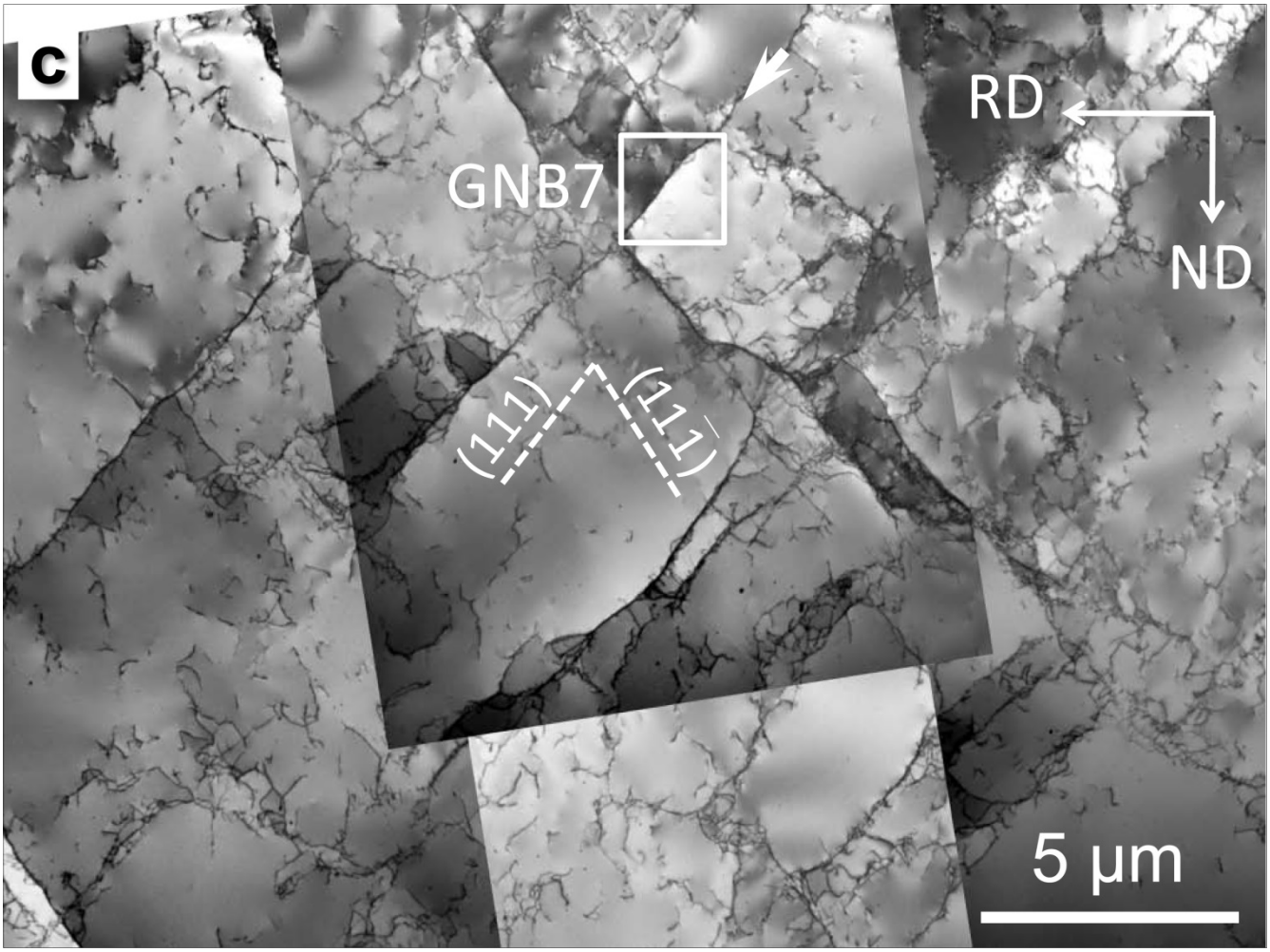

Figure 4 Relatively low-magnification images of individual GNBs. (a,b) Rolling-plane section at tilt positions near -35°. (c) Longitudinal section near zero tilt. Individual GNBs chosen for more detailed investigation are indicated by arrows and labeled.

Postprint
Philosophical Magazine, 2013 Vol. 93, No. 23, 3118–3141,
http://dx.doi.org/10.1080/14786435.2013.805270

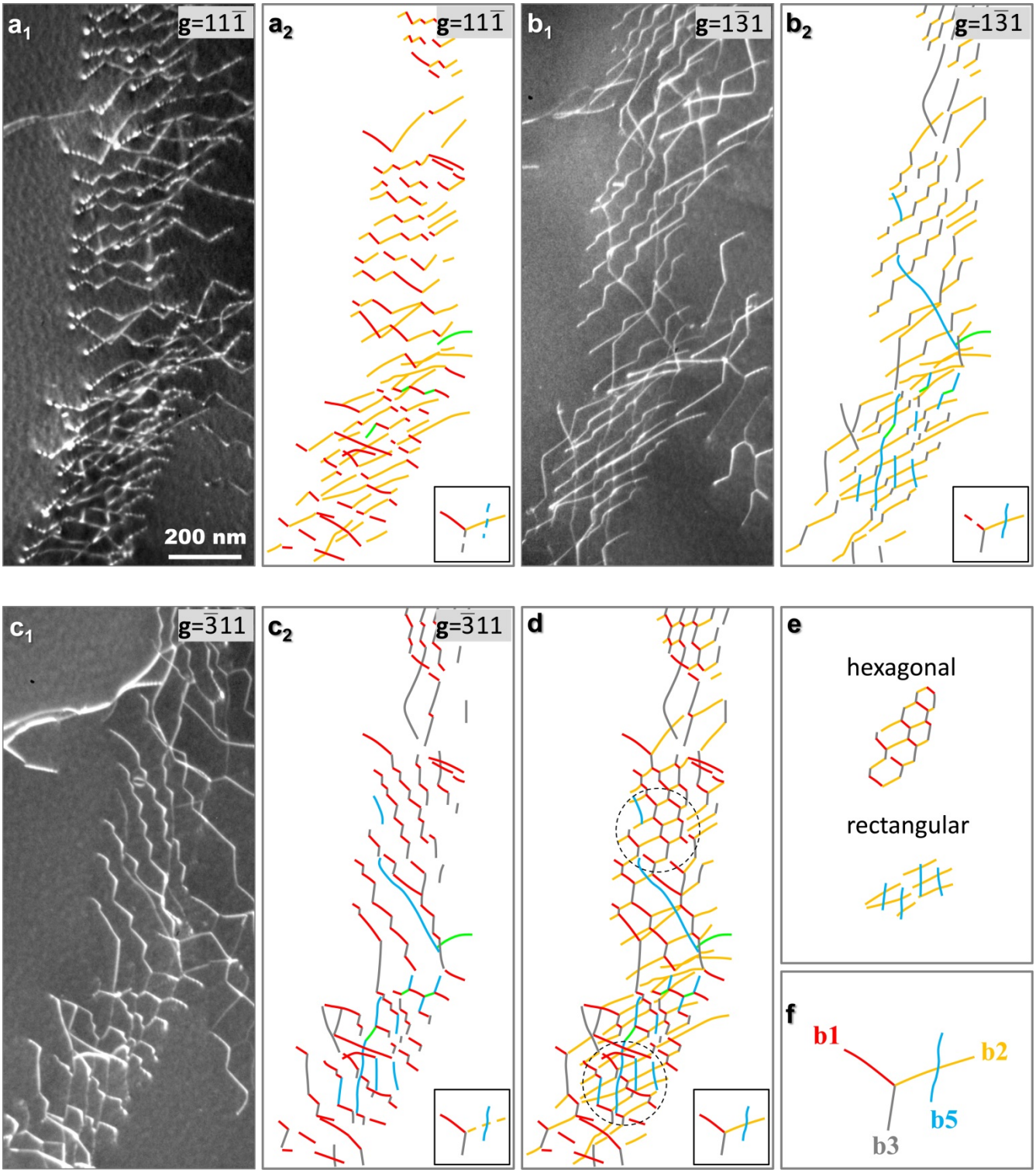

Figure 5 Determination of dislocation content of GNB2. (a_1,b_1,c_1) Example weak-beam images using **g**=[11$\bar{1}$], **g**=[1$\bar{3}$1] and **g**=[$\bar{3}$11], respectively. (a_2,b_2,c_2) Tracings of visible dislocations of (a_1), (b_1) and

Postprint
Philosophical Magazine, 2013 Vol. 93, No. 23, 3118–3141,
http://dx.doi.org/10.1080/14786435.2013.805270

(c_1), respectively. The lower-right insets indicate dislocation visibilities, where solid lines represent visible dislocations and dashed lines represent invisible ones. (d) Illustration of all identified dislocations. (e) Two typical dislocation configurations extracted from the circled regions in (d). (f) Elemental dislocations of (d). Three-dimensional arrangement of the dislocations is shown in supplementary Movie S2.

Postprint
Philosophical Magazine, 2013 Vol. 93, No. 23, 3118–3141,
http://dx.doi.org/10.1080/14786435.2013.805270

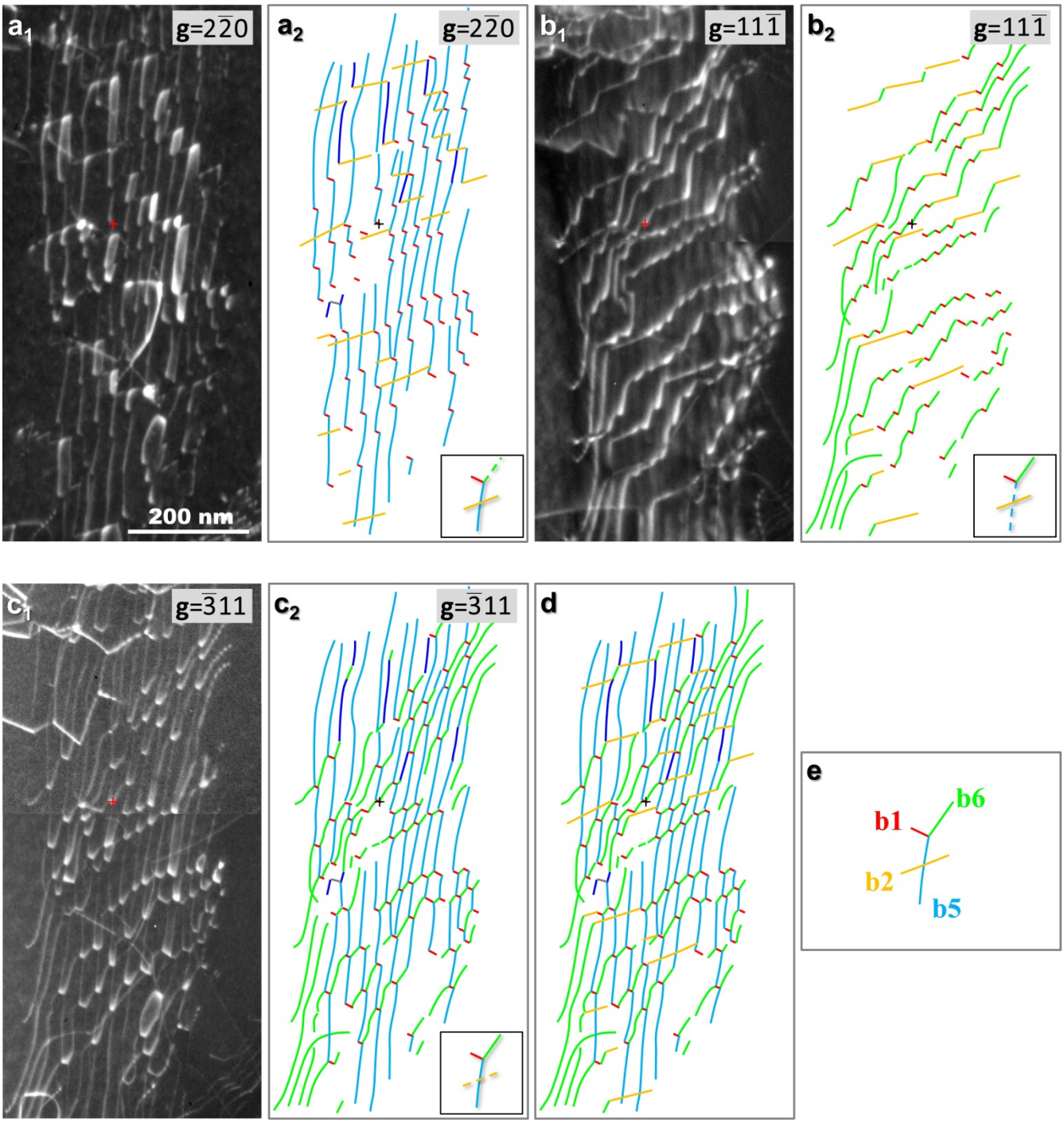

Figure 6 Determination of dislocation content of GNB3. (a_1,b_1,c_1) Example weak-beam images using **g**=[2 $\bar{2}$ 0], **g**=[11 $\bar{1}$] and **g**=[$\bar{3}$ 11], respectively. (a_2,b_2,c_2) Tracings of visible dislocations of (a_1), (b_1) and

(c_1), respectively. The lower-right insets indicate dislocation visibilities, where solid lines represent visible dislocations and dashed lines represent invisible ones. (d) Illustration of all identified dislocations. (e) Elemental dislocations of (d). Three-dimensional arrangement of the dislocations is shown in supplementary Movie S3.

Postprint
Philosophical Magazine, 2013 Vol. 93, No. 23, 3118–3141,
http://dx.doi.org/10.1080/14786435.2013.805270

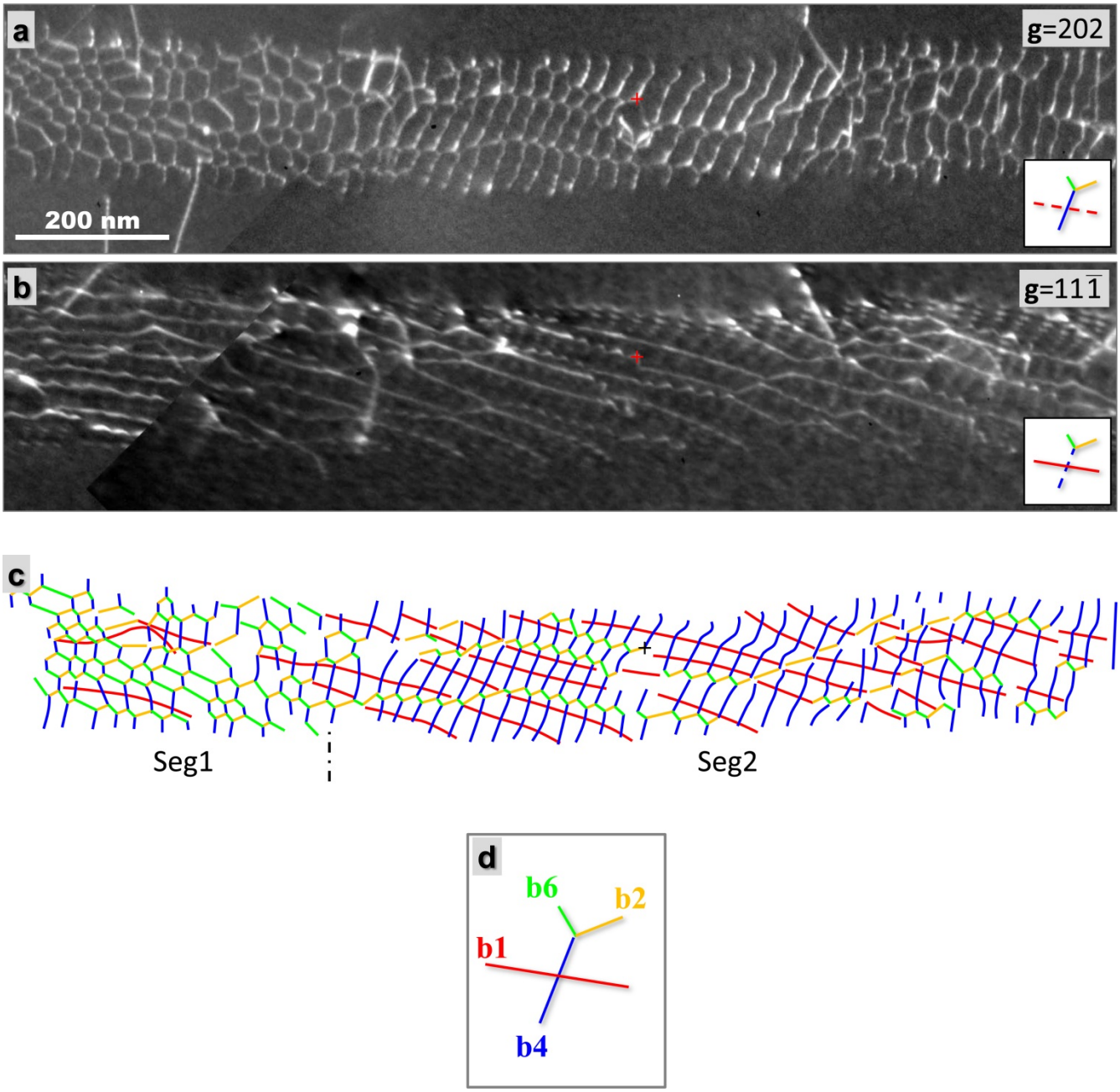

Figure 7 Determination of dislocation content of GNB7. (a,b) Example weak-beam images using **g**=[202] and **g**=[11$\bar{1}$], respectively. The lower-right insets indicate dislocation visibilities, where solid lines represent visible dislocations and dashed lines represent invisible ones. (c) Illustration of all identified dislocations. Two smaller planar segments of the boundary, namely Seg1 and Seg2, are indicated. (d) Elemental dislocations of (c).

Postprint
Philosophical Magazine, 2013 Vol. 93, No. 23, 3118–3141,
http://dx.doi.org/10.1080/14786435.2013.805270

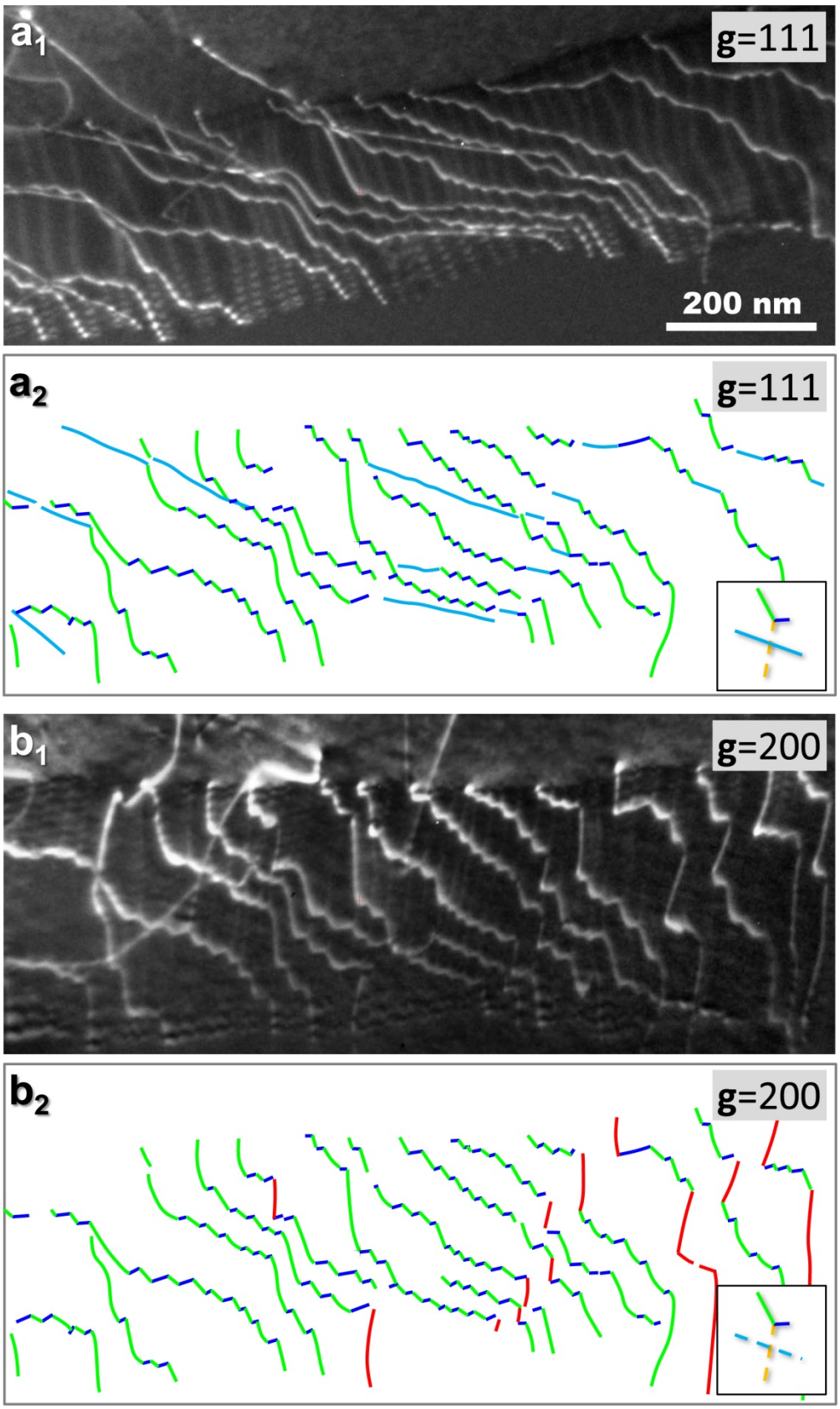

Postprint
Philosophical Magazine, 2013 Vol. 93, No. 23, 3118–3141,
http://dx.doi.org/10.1080/14786435.2013.805270

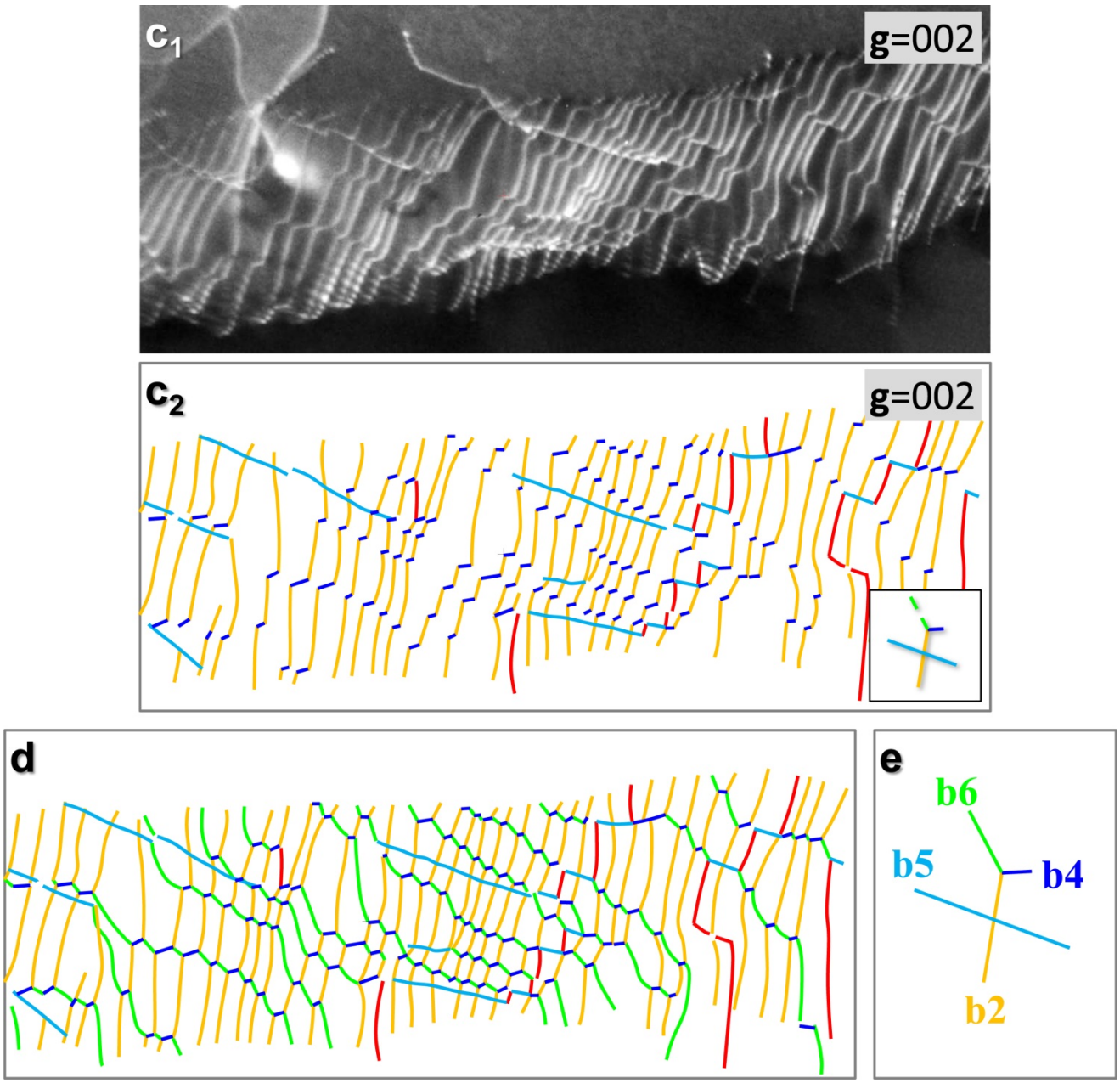

Figure 8 Determination of dislocation content of GNB8. (a_1,b_1,c_1) Example weak-beam images using **g**=[111], **g**=[200] and **g**=[002], respectively. (a_2,b_2,c_2) Tracings of visible dislocations of (a_1), (b_1) and (c_1), respectively. The lower-right insets indicate dislocation visibilities, where solid lines represent visible dislocations and dashed lines represent invisible ones. (d) Illustration of all identified dislocations. (e) Elemental dislocations of (d).

Postprint
Philosophical Magazine, 2013 Vol. 93, No. 23, 3118–3141,
http://dx.doi.org/10.1080/14786435.2013.805270

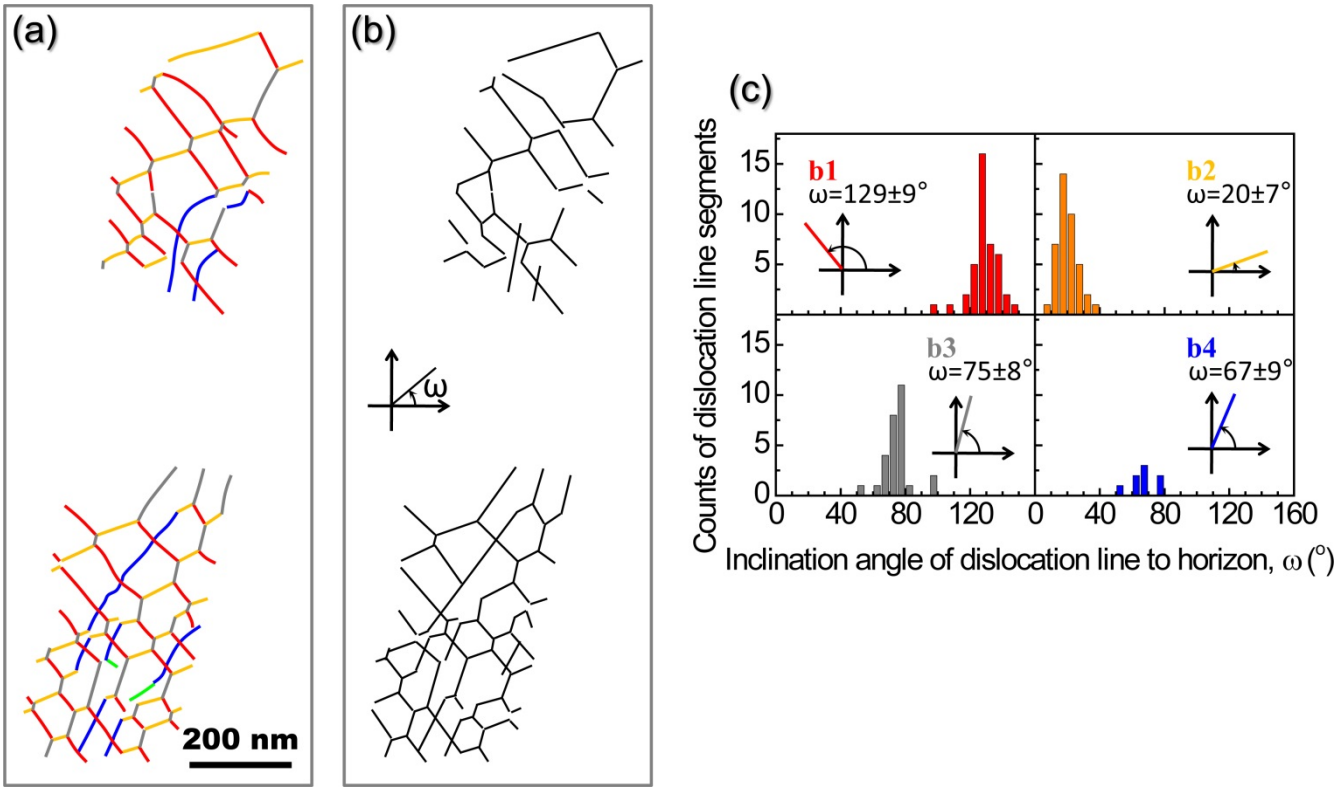

Figure 9 Determination of dislocation trace directions on a projected image for the dominant planar segments of GNB1. (a) Dislocation tracings from corresponding weak-beam images. (b) Linear segmentation of the dislocation tracings in (a). (c) Statistic distribution of dislocation trace directions for each set of dislocations shown in (a), in terms of the inclination angle to image horizon, ω, as measured from (b). The average value and standard deviation are given for each set of dislocations in (c). Three-dimensional arrangement of the dislocations is shown in supplementary Movie S1.

Postprint
Philosophical Magazine, 2013 Vol. 93, No. 23, 3118–3141,
http://dx.doi.org/10.1080/14786435.2013.805270

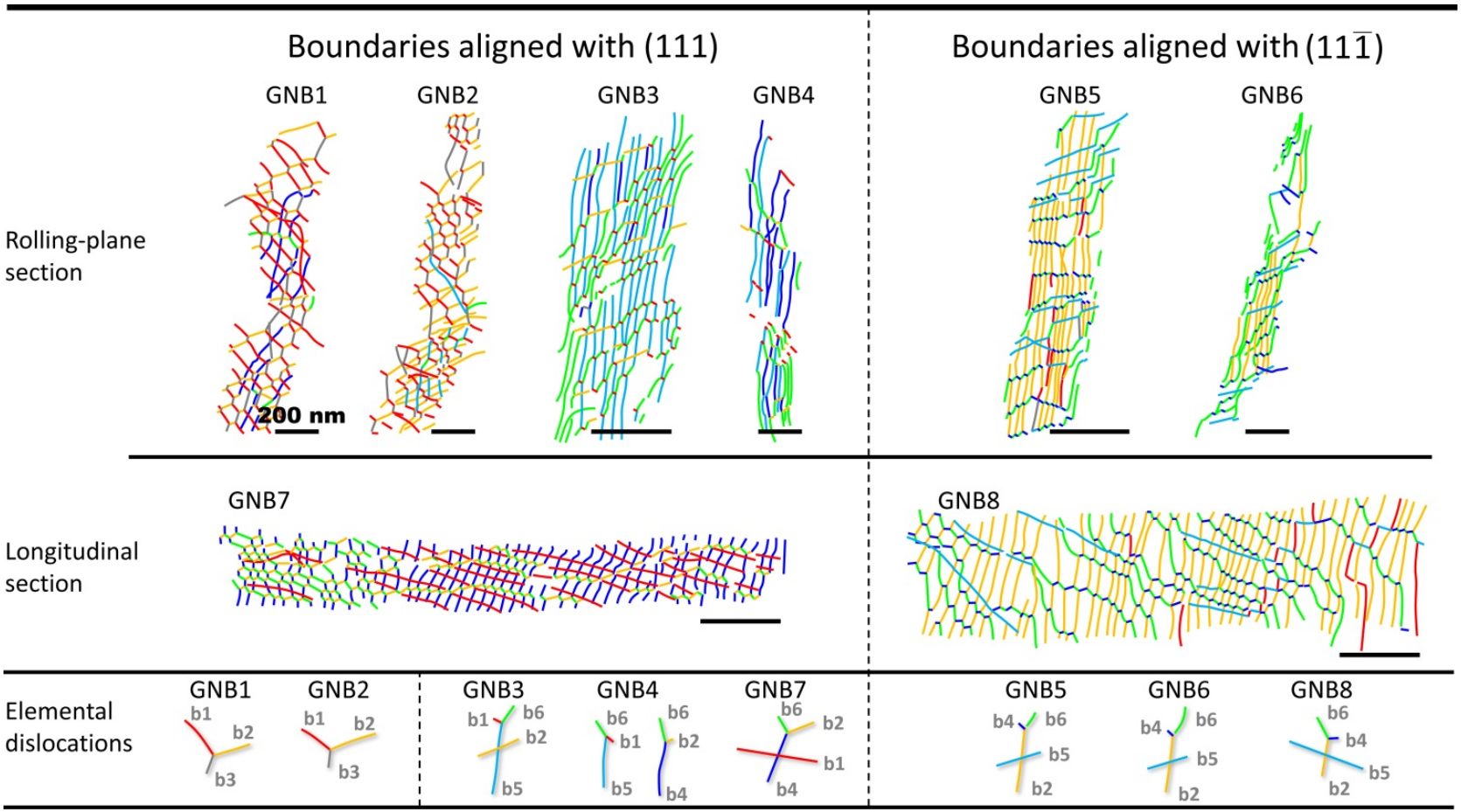

Figure 10 Summary of dislocation content of the GNBs. Scale bars correspond to 200 nm.

Postprint
Philosophical Magazine, 2013 Vol. 93, No. 23, 3118–3141,
http://dx.doi.org/10.1080/14786435.2013.805270

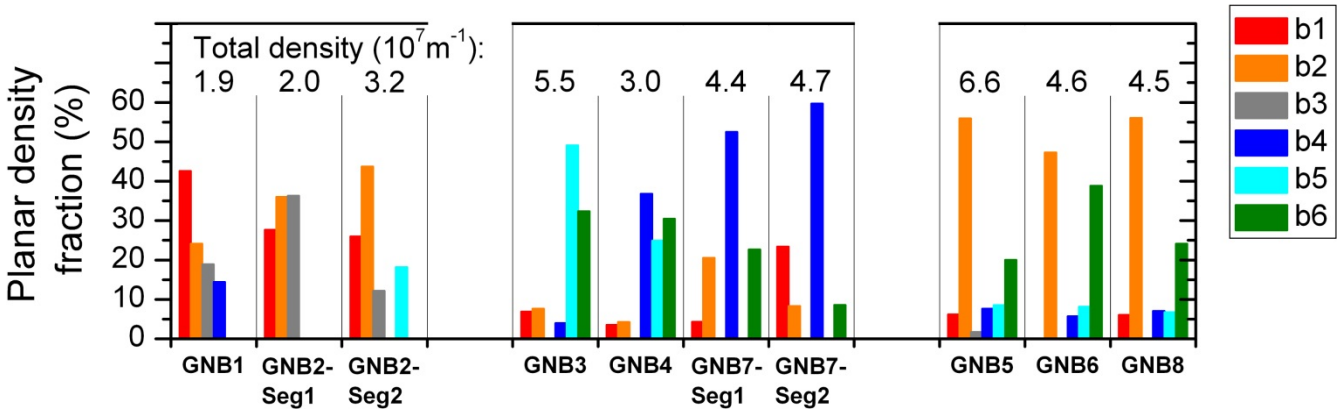

Figure 11 Planar dislocation densities of the GNBs corresponding to Fig. 10. For each GNB segment, the total planar dislocation density is indicated, and the fraction of each set of dislocations within the boundary is plotted.

Postprint
Philosophical Magazine, 2013 Vol. 93, No. 23, 3118–3141,
http://dx.doi.org/10.1080/14786435.2013.805270

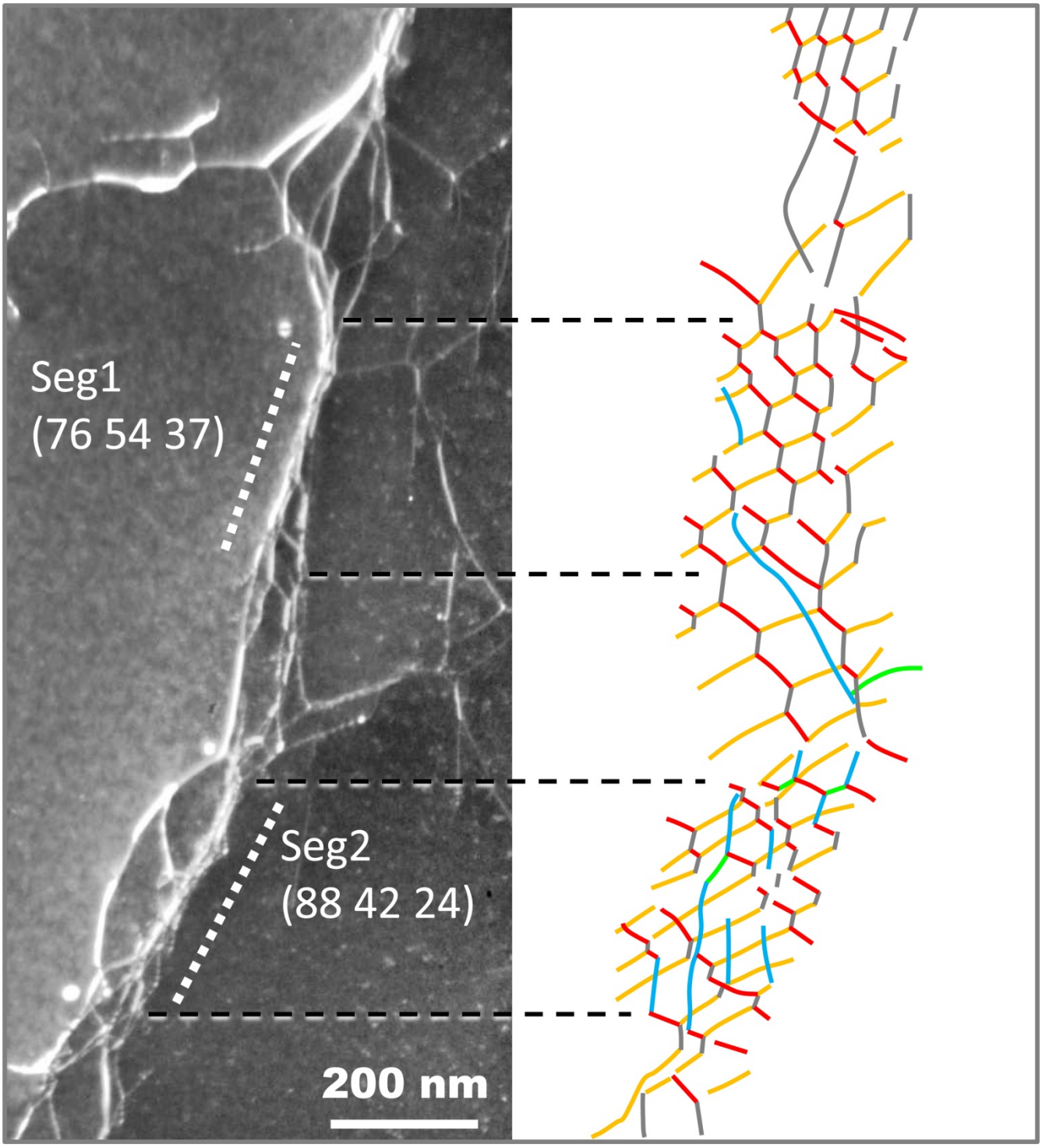

Figure 12 Correlation between variation of boundary plane and variation of dislocation content, an example from GNB2.